ACS NANO

www.acsnano.org

ARTICLE

Transparent Intracellular Sensing Platform with Si Needles for Simultaneous Live Imaging

Woohyun Park, Eun Mi Kim, Yale Jeon, Junsang Lee, Jonghun Yi, Jinheon Jeong, Bongjoong Kim, Byeong Guk Jeong, Dong Rip Kim,* Hyunjoon Kong,* and Chi Hwan Lee*

Cite This: *ACS Nano* 2023, 17, 25014–25026

Read Online

ACCESS | Metrics & More | Article Recommendations | Supporting Information

ABSTRACT: **Vertically ordered Si needles are of particular interest for long-term intracellular recording owing to their capacity to infiltrate living cells with negligible damage and minimal toxicity. Such intracellular recordings could greatly benefit from simultaneous live cell imaging without disrupting their culture, contributing to an in-depth understanding of cellular function and activity. However, the use of standard live imaging techniques, such as inverted and confocal microscopy, is currently impeded by the opacity of Si wafers, typically employed for fabricating vertical Si needles. Here, we introduce a transparent intracellular sensing platform that combines vertical Si needles with a percolated network of Au−Ag nanowires on a transparent elastomeric substrate. This sensing platform meets all prerequisites for simultaneous intracellular recording and imaging, including electrochemical impedance, optical transparency, mechanical compliance, and cell viability. Proof-of-concept demonstrations of this sensing platform include monitoring electrical potentials in cardiomyocyte cells and in three-dimensionally engineered cardiovascular tissue, all while conducting live imaging with inverted and confocal microscopes. This sensing platform holds wide-ranging potential applications for intracellular research across various disciplines such as neuroscience, cardiology, muscle physiology, and drug screening.**

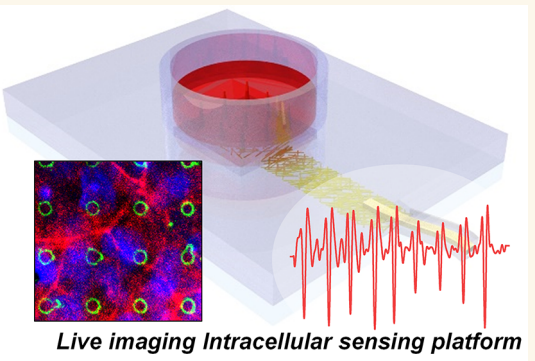

KEYWORDS: *Intracellular recording, intraorganoid sensing, live cell imaging, microneedle, nanowires*

INTRODUCTION

Intracellular recording is pivotal in deepening the understanding of cellular function, promoting therapeutic development, advancing drug discovery, and stimulating technological innovation in a range of fields, including neuroscience, cardiology, muscle physiology, and drug screening.[1−6] Patch-clamp techniques remain the current gold standard for intracellular recording, providing high-fidelity recordings of cellular activity.[7] However, the invasive nature of patch-clamp techniques limits their widespread applications in many fields.[8] An alternative approach involves utilizing vertically ordered one-dimensional (1D) nanostructures, such as wires, needles, pillars, straws, and tubes, at cellular and subcellular length scales to serve as bioprobes with high spatial resolution.[9−14] Compared to other options, Si needles are of particular interest for intracellular recording due to their minimal invasiveness, low toxicity to cells, and compatibility with traditional nanofabrication processes.[15−20]

Real-time live imaging, often combined with the direct recording of electrical signals from electrodes, is a crucial component of intracellular recording, enabling the visualization of cellular and subcellular morphology with a high level of specificity.[21−23] In addition to providing valuable insights into the location and behavior of recorded cells, live imaging offers a comprehensive understanding of the underlying cellular processes being studied. Access to this information enables researchers to gain a deeper understanding of the intricate physiological functions and signaling pathways of cells, thereby enhancing the precision and dependability of intracellular recording.[24−27] However, standard live imaging techniques, such as inverted and confocal microscopes, require inverting the device or using planar microelectrode arrays on transparent substrates, which are typically limited to recording extracellular signals.[28−31] Vertically ordered Si needles have yet to be implemented due to the opacity of Si wafers typically employed for fabricating vertical Si needles. Furthermore, the rigidity of Si wafers may cause mechanical discrepancies with cells during intracellular recordings, leading to cell stress and

Received: August 11, 2023
Revised: November 29, 2023
Accepted: December 4, 2023
Published: December 7, 2023

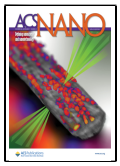

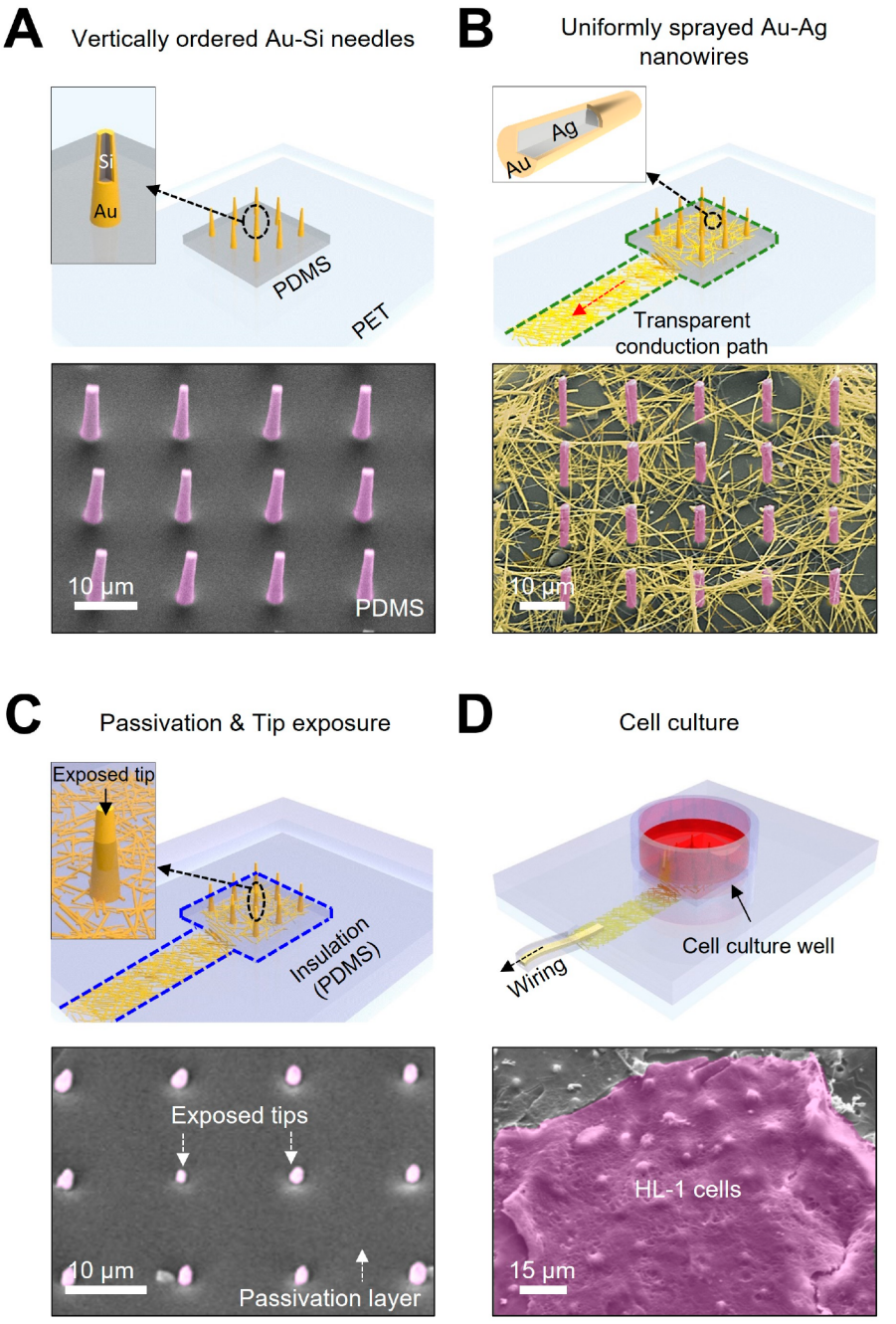

Figure 1. Schematic illustrations (top panel) and SEM images (bottom panel) detailing the fabrication of the platform, including: (A) the assembly of vertical Si needles on PDMS and PET film, (B) the application of Ag−Au NW via spray coating to enhance conductivity, (C) insulation and tip exposure achieved through PDMS spin-coating and plasma etching, and (D) the cultivation of an HL-1 cell monolayer on the vertical Si needles.

damage that can impair the quality of intracellular signals.[32] Therefore, it is necessary to integrate vertical Si needles onto a transparent and flexible substrate, thereby facilitating simultaneous intracellular recording and imaging with minimal invasiveness.

Here, we introduce a transparent intracellular sensing platform that combines vertical Si needles with a percolated network of Au−Ag nanowires on a transparent elastomeric substrate. This sensing platform offers key features, including: (1) a low electrochemical impedance, measuring less than 110 Ω cm^2 at 1 kHz, which remains stable for over 28 days of intracellular recording; (2) excellent optical transparency exceeding 80% in the 400−700 nm range, facilitating standard live imaging techniques such as inverted and confocal microscopes; (3) mechanical compliance that permits Si needles to interface with cells without the risk of fracture or delamination from the substrate; and (4) outstanding cell viability, exceeding 99%. Taken together, these features render this sensing platform suitable for simultaneous intracellular recording and imaging. Proof-of-concept demonstrations include recording intracellular electrophysiology from different types of cells, such as cardiomyocytes and 3D-engineered cardiovascular tissue,[33] during live imaging before and after the administration of therapeutic drugs. As such, this sensing

https://doi.org/10.1021/acsnano.3c07527
ACS Nano 2023, 17, 25014−25026

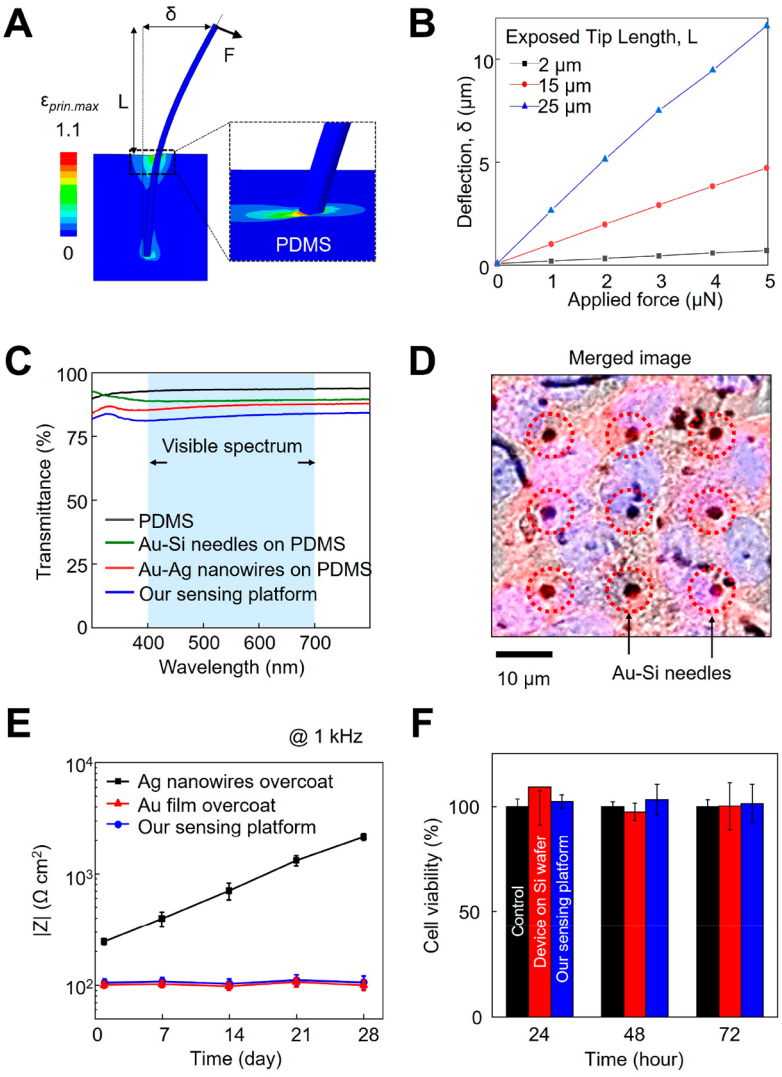

Figure 2. (A) FEA results displaying the strain distribution (ε) and deflection (δ) of a single vertical Si needle on a PDMS substrate with Ag−Au nanowires, under a contraction force (F) of 5 μN exerted by a cell. (B) FEA results illustrating its deflection (δ), considering varying applied forces and an exposed length (L). (C) Optical transmittance measurements for various configurations including bare PDMS, vertical Si needles on PDMS, Ag−Au nanowires on PDMS, and our sensing platform. (D) DIC, confocal, and merged images showing an HL-1 cell on our sensing platform. (E) Illustration of changes in electrochemical impedance in our sensing platform relative to controls, measured at 1 kHz over time, during immersion in PBS and incubation at 37 °C with 5% CO_2. Data is represented as the mean ± standard deviation, with n = 5 for each group. (F) Presentation of cell viability results for our sensing platform in comparison to controls, depicted as the mean ± standard deviation, with n = 5 for each group.

platform holds the potential to advance drug screening and therapies for cardiovascular or other diseases by facilitating comprehensive electrical and optical monitoring of cellular activity over time.

RESULTS AND DISCUSSION

Transparent Intracellular Sensing Platform. The fabrication of the transparent intracellular sensing platform began with a Si wafer. Vertically ordered Si needles were created on this wafer through photolithographic patterning and deep reactive ion etching (DRIE). The Si needles were then coated with a thin, 50 nm-thick layer of Au and subsequently transfer printed onto an elastomeric substrate, such as polydimethylsiloxane (PDMS). To ensure minimal invasiveness when introduced into cells, the Si needles were designed to taper from a base diameter of <2 μm at the bottom to a tip diameter of <900 nm at the top.[32,34,35] Surface area was increased to decrease impedance, achieved by texturing the surface of the Si needles with nanopores.[36,37] These nanopores, with diameters ranging from 5 to 20 nm, led to an overall porosity of 30%. Details of the fabrication processes are described in the Experimental Methods section and also illustrated in Supplementary Figure S1.

Figure 1 provides schematic illustrations (top panel) and scanning electron microscope (SEM, bottom panel) images of the subsequent fabrication processes to complete our sensing platform. First, the PDMS substrate, consisting of Au-coated Si (Au−Si) needles, was bonded to a polyethylene terephthalate (PET) film to serve as a handling carrier (Figure 1A). Second, Au-coated Ag (Au−Ag) nanowires were prepared and uniformly sprayed for 15 s across the surface of the PDMS substrate with a shadow mask to define a transparent

https://doi.org/10.1021/acsnano.3c07527
ACS Nano 2023, 17, 25014−25026

conduction path leading to a connection pad (Figure 1B).[38] The SEM image highlights the percolated network of Au−Ag nanowires in contact with the Au−Si needles, establishing an electrical connection. The surface of the Au−Ag nanowires was treated with (3-aminopropyl) triethoxysilane (APTES) prior to spraying to improve adhesion, and was also chemically welded after spraying to reduce sheet resistance to 36.81 ± 0.93 Ω sq^{-1} (Figure S2).[39,40] Details on the synthesis and implementation of the Au−Ag nanowires are listed in the Experimental Methods section. Next, a diluted PDMS solution was spin-cast over the surface using a thinner solution (Smooth-On, NOVOCS Gloss Silicone Solvent) at a weight ratio of 1:10 to fully passivate the Au−Ag nanowires for electrical insulation, followed by a reactive ion etching (RIE) process to expose the tips of the Au−Si needles. The SEM image highlights the passivation layer with the exposed tips of the Au−Si needles. The length of the exposed tips was controlled by adjusting the RIE time in a range of approximately 2 to 25 μm (Figure S3). Finally, a cell culture well, made of PDMS, was affixed surrounding the exposed tips, enabling cell culture (Figure 1D). The SEM image displays a confluent layer of mouse cardiomyocyte (HL-1) cells (in magenta), interfacing with the exposed tips after 3 weeks of cell culture in a phosphate buffer solution (PBS) at 37 °C.

Mechanical, Electrical, and Optical Characterizations. Our sensing platform is mechanically compliant, electrically conductive, and optically transparent, which are critical for simultaneous intracellular recording and imaging. Figure 2A presents the finite element analysis (FEA) results of strain distribution (ε) and deflection (δ) for a single Au−Si needle interacting with a cell under a contraction force (F) of 5 μN. Details of the modeling parameters are described in the Experimental Methods section. The peak principal strains appeared on the top surface of the PDMS substrate surrounding the Au−Si needles, opposite the direction of the applied force. Consistent results were obtained as the applied force increased up to 5 μN, and the exposed tip length (L) of the Au−Si needles increased from 2 to 15 μm and then to 25 μm, with a corresponding increase in deflection (Figure 2B). The spring constant of the Au−Si needles was determined to be 1.86, 0.35, and 0.14 N m^{-1} for L = 2, 15, and 25 μm, respectively. The corresponding FEA results for the principal strain and stress distributions at L = 2 μm, 15 μm, and 25 μm are shown in Supplementary Figure S4 and Movie S1. The embedded length of the Au−Si needles into the PDMS substrate had the ability to rotate, rather than just bend, due to elastic compliance at the interface, which could substantially reduce the strain applied to the Au−Si needles as compared to that built on a rigid substrate such as a Si wafer (Figure S5). The Au−Si needles on the PDMS substrate experienced a maximum Mises stress of <1.2 GPa, which is lower than that of the same needle on a Si wafer (approximately 2 GPa). These findings indicate that the Au−Si needles on the PDMS substrates may help reduce the risk of fractures or delamination during cell interactions, a conclusion that is in line with experimental observations.

Figure 2C displays the optical transmittance of our sensing platform in the visible spectrum (400−700 nm), which measures >80% compared to the control samples, including a bare PDMS, the Au−Si needles on PDMS, and a percolated network of the Au−Ag nanowires on PDMS. The density of the Au−Ag nanowires was increased by spraying them for durations ranging from 5 to 30 s, resulting in a slight decrease in optical transmittance and an exponential decrease in sheet resistance (Figure S6A). To optimize both optical transmittance and sheet resistance of our sensing platform, the Au−Ag nanowires were sprayed for 15 s, resulting in an optical transmittance of >80% and a sheet resistance of <100 Ω sq^{-1}. Representative inverted microscope images of our sensing platform with and without the Au−Ag nanowires, sprayed for 15 s, are shown in Supplementary Figure S6B, which were obtained through its optical transparency. Figure 2D presents a merged image of differential interference contrast (DIC) and confocal microscopy of HL-1 cells in conjunction with the Au−Si needles, revealing targeted cellular structures such as cell membranes (in red) and nuclei (in blue). The separate DIC and confocal images are shown in Supplementary Figure S6C. Inverted and confocal microscopes were utilized to obtain these real-time, label-free images, which are feasible only with the presence of a transparent substrate.

Figure 2E shows the electrochemical impedance of our sensing platform immersed in PBS at a frequency of 1 kHz over a 28-day period, while being incubated at 37 °C and 5% carbon dioxide (CO_2). For comparison, control groups included the Si needles coated with (1) a 50 nm-thick Au film applied via sputtering and (2) a percolated network of Ag nanowires, both set on a Si wafer (Figure S7). The results reveal that our sensing platform, as well as the control device coated with the Au film, maintained a nearly unchanged impedance, fluctuating within a narrow range of only 5.3%. This included readings of 103.25 ± 6.21 Ω cm^2 on day 0 to 102.78 ± 10.63 Ω cm^2 on day 28, and 105.15 ± 8.28 Ω cm^2 on day 0 to 109.77 ± 14.17 Ω cm^2 on day 28, respectively (n = 5 for each group). On the other hand, the control device coated with Ag nanowires experienced a significant impedance increase, from 250.53 ± 15.88 Ω cm^2 on day 0 to 2,150.98 ± 155.14 Ω cm^2 on day 28. Additionally, the electrochemical impedance of our sensing platform ($|Z|$ = 105.1 ± 4.4 Ω cm^2) remained similar to that of the control device coated with the Au film (97.3 ± 5.8 Ω cm^2) at 1 kHz in PBS (Figure S8). The phase shift data suggested that both our sensing platform and the control device coated with the Au film behaved like parallel resistor-capacitor (RC) circuits. The cyclic voltammetry analysis suggested that our sensing platform demonstrated a total charge storage capacity of 0.51 ± 0.33 mC cm^{-2}, significantly higher than that (0.04 ± 0.10 mC cm^{-2}) of the control device coated with Ag nanowires, but slightly lower than that (0.66 ± 0.39 mC cm^{-2}) of the control device coated with the Au film (n = 5 for each group). Overall, our sensing platform exhibited electrical characteristics comparable to those of previously reported platforms that used Au nanowires as electrodes.

To ensure long-term reliable intracellular recording, our sensing platform is required to provide high cell viability. To this end, the Ag nanowires that were used in our sensing platform were fully covered with a thin layer of Au to prevent the release of toxic Ag ions into the surrounding medium.[38,41] Figure 2F displays the cell viability results of our sensing platform with HL-1 cells at 24, 48, and 72 h, as determined by an MTT assay (3-(4,5-dimethylthiazol-2-yl)-2,5-diphenyltetrazolium bromide), when the length of the exposed tip was maintained around 5 μm. The cell viability of our sensing platform remained consistently above 99% throughout the assay period, with no significant differences observed between groups (n = 5 for each group). Generally, the diameter and height of the needle and the density of the array correlate

https://doi.org/10.1021/acsnano.3c07527
ACS Nano 2023, 17, 25014−25026

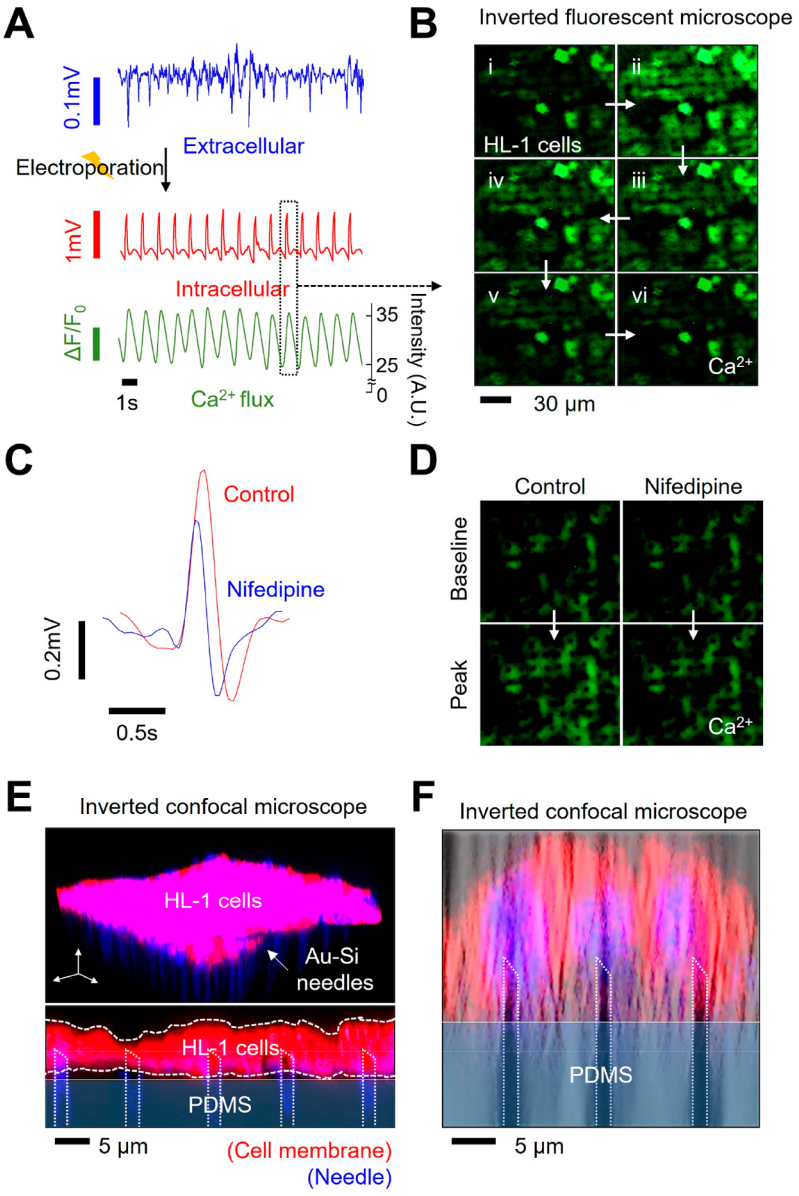

Figure 3. (A) Recordings of HL-1 action potential, showing extracellular signals (blue) prior to electroporation and intracellular signals (red) following electroporation, along with the simultaneous recording of calcium flux measurement (green). (B) Snapshots from a video capturing the changes in HL-1 calcium flux during a single action potential. (C) Effects of the ion channel-blocking drug nifedipine. (D) Imaging of calcium flux, showing baseline and peak levels before and after treatment with nifedipine. (E) 3D (top) and cross-sectional (bottom) images, labeled with cell membrane (red) and vertical Si needles (blue), to demonstrate the tight interface created between the vertical Si needles and the cell membrane. (F) DIC image merged with confocal imaging shows the vertical Si needles (gray) are overlapped with membrane (red) and nucleus (blue).

positively with the penetration force applied to the cell, affecting cell viability.[42−44] The density of the needle array, as well as cell viability, is related to the interface tightness and stress between the cell and the sensing patch, which in turn influence penetration behavior and the quality of the recorded electrical signal.[44,45] Previous research, including papers from our group, has shown successful cell tests with needle diameters ranging from 80 nm to 3 μm and heights from 700 nm to 70 μm, covering the proposed geometry in this paper. No significant differences in cell viability associated with changes in the diameter and length of the needle were observed.[32,34,35,46] The excellent cell viability of our sensing platform after 72 h of culture was also confirmed using the Calcein AM assay (Figure S9A). Furthermore, confocal microscope images revealed that our sensing platform supported HL-1 growth, with the cells reaching confluency and exhibiting beating activity, as evidenced by the actin (green) and nucleus (blue) staining (Figure S9B).

Simultaneous Intracellular Recording and Imaging with Cardiomyocyte Cells. To demonstrate the capability of our sensing platform in simultaneous intracellular recording and imaging, we cultured HL-1 mouse cardiomyocytes until they reached confluency and exhibited spontaneous beating. The surface of our sensing platform was coated with a gelatin solution to ensure cell adhesion, and no additional functionalization agents were used. The HL-1 cells were

https://doi.org/10.1021/acsnano.3c07527
ACS Nano 2023, 17, 25014−25026

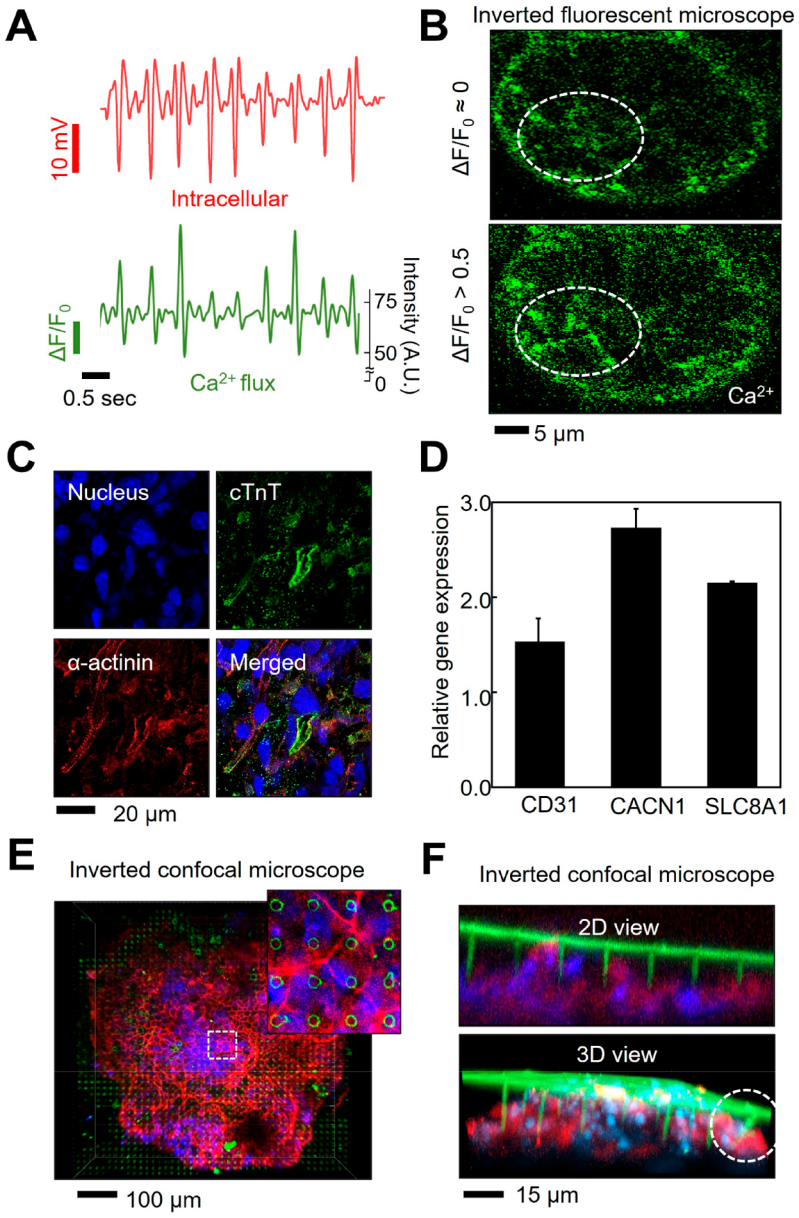

Figure 4. (A) Intraorganoid field potential measurement (red) along with a simultaneous recording of calcium flux measurement (green). (B) Fluorescence images of calcium flux within cells from cardiovascular organoids. (C) Fluorescence images that reveal the expression of cTnT and α-actinin in cardiovascular organoids. (D) Relative gene expression of cardiovascular and calcium handling markers in cells from cardiovascular organoids, normalized to cells from embryonic bodies, with n = 10 for each group. (E) 3D images of a cardiovascular organoid interfacing with the vertical Si needles, stained for actin (red), nucleus (blue), and vertical Si needles (green). (F) Cross-sectional (top) and 3D (bottom) views of the vertical Si needles placed into the cardiovascular organoid, with staining for actin (red), nucleus (blue), and vertical Si needles (green). A white dotted circle illustrates the flexible nature of the vertical Si needles, showing how they are buckled toward the organoid.

cultured for 3−5 days until they achieved confluency and exhibited spontaneous beating (Movie S2). Initially, extracellular action potentials with amplitudes less than 0.1 mV were detected (Figure 3A, top panel). To further improve the adhesion of the Au−Si needles to the cell membrane, mechanoporation was conducted by centrifuging at 500 rpm for 1 min.[47−49] Electroporation was followed using a series of biphasic square pulses to facilitate electrical access to the intracellular region.[9,10] Details of the mechanoporation and electroporation parameters are described in the Experimental Methods section. The beating interval remained at the same level before and after mechanoporation and electroporation, with the amplitude increasing drastically by 10× up to 1 mV and a significantly reduced noise level (Figure 3A, middle panel). In order to showcase the live imaging capabilities through the optical transparency of our sensing platform, concurrent calcium ion (Ca^{2+}) flux imaging was simultaneously performed using an inverted microscope - a standard tool that is compatible only with transparent substrates (Movie S3). For Ca^{2+} flux imaging, Fluo-8, a fluorescent calcium indicator, was loaded into the cells for live imaging, and the alteration in the fluorescent intensity (ΔF) was measured and compared with the resting intensity (F_0). The Ca^{2+} flux imaging is a well-established technique used to monitor the activity of

https://doi.org/10.1021/acsnano.3c07527
ACS Nano 2023, 17, 25014−25026

electrogenic cells by tracking the changes in calcium flux evoked by action potentials.[50−52] Figure 3A (bottom panel) depicts the measured change in Ca^{2+} flux, demonstrating synchronized beating with electrical measurement at a frequency of 1 Hz.

Figure 3B presents the inverted fluorescent microscope images taken during a single action potential, showing a distinct peak of calcium ions upon depolarization through the opening of L-type calcium channels, enabling Ca^{2+} to enter the cell down its concentration gradient, followed by subsequent recovery through repolarization by the closing of the calcium channel. To evaluate the signal quality of our sensing platform, a comparative analysis of signal amplitude was conducted in comparison to that of a control group including the Au−Si needles on a Si wafer. The measurements were limited to the cells that had been beating at approximately 1 Hz for at least 1 day, as the recorded amplitude and beating interval can vary with cell culture age. The action potentials of the cells were recorded using our sensing platform (n = 25), yielding an average amplitude of 1.30 ± 0.43 mV. Under the same conditions, the intracellular action potentials of the cells were recorded using the control group (n = 25), yielding an average amplitude of 1.29 ± 0.31 mV. The measured peak amplitudes were not significantly different. These findings indicate that our sensing platform offers similar capabilities for intracellular recording as the control group while also providing mechanical compliance and optical transparency allowing for both reliable recording and simultaneous imaging.

To further demonstrate its utility in drug screening, 100 nM of an ion channel blocking drug nifedipine was administered to the cells to observe changes in action potential morphologies. Nifedipine is known to block L-type Ca^{2+} channels, thereby hindering the influx of Ca ions into the intracellular region, resulting in early repolarization and a reduction in peak amplitude.[53] Figure 3C shows that the amplitude was lowered and the action potential duration was reduced compared to the control signal without administering the drug. Specifically, the action potential duration at 50% of repolarization (APD50) decreased significantly from 120.05 ± 13.02 ms to 104.80 ± 7.42 ms, while the peak amplitude showed a significant decrease from 0.85 ± 0.17 to 0.55 ± 0.12 mV (Figure S11). Additionally, the Ca^{2+} flux imaging shows that intensity decreased at the peak level after nifedipine treatment from 2.8 to 2.4 $\Delta F/F_0$, aligning with the intracellular recording data (Figure 3D), representing a composite signal from multiple cells. Both the electrical and optical measurements of the change in action potential align with previous studies on nifedipine, highlighting the potential use of our sensing platform in drug screening.[54−56]

The ability of the Au−Si needles to penetrate the cell membrane and provide intracellular access was confirmed by using fluorescent labeling with an inverted confocal microscope (Figure 3E). The 3D and cross-sectional images, labeled with the cell membrane (in red) and needles (in blue), demonstrate the tight interface formed between the Au−Si needles and the cell membrane. The distance between the HL-1 cells and the PDMS layer was evaluated, resulting in an average of 0.13 μm with a standard deviation of 0.073 μm, through the analysis of the confocal image representing a signal-to-noise ratio of −4.6 dB. Figure 3F shows a representative merged image (split channel images, Figure S12) obtained from both DIC and confocal microscope, showing the overlapped configuration of Au−Si needles and nucleus. The penetration of the Au−Si needles all the way through the cell cytoplasm can be confirmed on the combined basis of amplitude increase in electrical signal and cross-sectional confocal images.

Simultaneous Intracellular Recording and Imaging in 3D-Engineered Tissue. Over the past decade, significant strides have been made toward developing 3D organ-like structures.[57,58] These miniaturized organs mimic the multicellular composition, anatomy, and functionality of actual organs, providing a scaffold for investigating organ growth, maintenance, regeneration, and disease processes.[59−61] Furthermore, these structures expedite more accurate drug screening and toxicity testing, reducing costs and development times for new pharmaceuticals and healthcare products.[62,63] Utilizing various biosensors allows for real-time, minimally invasive monitoring of intercellular communication, revealing the influence of biochemical and biophysical environments on organ functionality.[64−67] This study showcases the potential utility of our sensing platform for simultaneous intracellular recording and imaging in 3D-engineered cardiovascular tissue. The intracellular function was assessed via field potential measurements during Ca^{2+} flux imaging. Details on the formation and characterization of the 3D-engineered cardiovascular tissue are described in the Experimental Methods section.

Figure 4A presents the measurement results of the intraorganoid field potential (top panel) and Ca^{2+} flux signal (bottom panel), with their clear synchronization observed every 0.5 s. Simultaneous imaging with an inverted fluorescence microscope confirmed that the Ca^{2+} flux signal from the 3D-engineered cardiac tissue consistently surpassed 0.5 $\Delta F/F_0$ (Figure 4B). The structural differences between 2D monolayered cells and 3D organoid cultures result in variations in the recorded signal. This is in addition to the differences stemming from the distinct measured parameters: intracellular action potential (Figure 3A) and intraorganoid field potential (Figure 4A). The synchronized data of the intracellular recording and imaging during the rhythmic beating of the engineered tissue are shown in Movie S4. After 14 days of differentiation, the 3D-engineered tissue expressed α-actinin and cardiac troponin T (cTnT). The organoid displayed a cardiac sarcomeric actin structure, including Z-disc and cTnT (Figure 4C), and exhibited increased gene expression of CD31, CACNA1C, and SLC8A1 compared to undifferentiated embryonic bodies (EBs) (Figure 4D), signifying successful cardiovascular differentiation. The disparities observed in the relationship between electrical and fluorescence recordings, as shown in Figures 3 and 4, can be attributed to the inherent differences in cell structures and the distinct recording methods employed for each.

Figure 4E presents a representative confocal microscope image of our sensing platform interfacing with the 3D cardiovascular tissue on top, stained with actin (in red) and the nucleus (in blue), captured through the transparent substrate. The inset image, acquired at a single focal plane, emphasizes the presence of the Au−Si needles within the 3D cardiovascular tissue. The Au−Si needles were placed into the 3D tissue, via gravity, after a resting period of approximately 5 min, as confirmed by the side view of the inverted confocal microscope images in both 2D and 3D views (Figure 4F and Figure S13). Notably, the Au−Si needles on the edge (white dotted circle) buckled due to its interaction with the nonlinear surface of the 3D tissue, without fracturing or delaminating,

https://doi.org/10.1021/acsnano.3c07527
ACS Nano 2023, 17, 25014−25026

owing to the mechanical compliance of our sensing platform in accommodating mechanical discrepancies.

CONCLUSIONS

In this study, we introduce a transparent intracellular sensing platform that combines vertically ordered Au−Si needles with a percolated network of Au−Ag nanowires on a transparent elastomeric substrate. This sensing platform offers low electrochemical impedance, high optical transparency, and excellent mechanical compliance and promotes cell viability, making it ideal for simultaneous intracellular recording and imaging. As a potential direction for future studies, the influence of cell confluency on action potential recordings and the long-term viability of cells postelectroporation can be investigated. Furthermore, assessing its applicability across various cell types involves addressing its strengths and limitations with a comprehensive optimization of needle geometry and density. These factors could also affect cell viability, behavior, and the signal-to-noise ratio.[42−45] The sensing platform can monitor intracellular electrophysiological functions over time, including cardiomyocytes and 3D-engineered cardiovascular tissue, and capture their functional changes upon administration of a therapeutic drug. Moreover, this sensing platform exhibits potential benefits for optogenetics, allowing light signals to traverse from both sides with notable efficiency, indicating a promising avenue for future research. This feature would not only support the investigation of cellular processes and responses to various stimuli but also enhance drug development, personalized medicine approaches, and the study of complex cellular interactions using light-based modulation techniques.

EXPERIMENTAL METHODS

Fabrication of Si Needles on a Si Wafer. The process of fabricating Si needles on a Si wafer involves several steps. First, a Si wafer (p-type, 525 μm thick, 0.001 to 0.005 Ω cm) was soaked in a buffered oxide etch solution (J. T. Baker Inc.) for one min to eliminate the native oxide layer. Next, a standard photolithographic patterning process was used in conjunction with deep reactive ion etching (DRIE) to produce vertically aligned Si pillars with predetermined diameters and depths. The DRIE process consisted of several deposition and anisotropic etching steps. During deposition step, a thin layer of $(C_xF_y)n$ polymer was deposited on the surface of the Si pillar to passivate it. This passivation layer was created using octafluorocyclobutane (C_4F_8) gas at a flow rate of 130 sccm and 800 W of radio frequency (RF) plasma power. Following the deposition step, the bottom surface of the Si wafer was anisotropically etched using sulfur hexafluoride (SF_6) gas at a flow rate of 85 sccm, 450 W of RF plasma power, and 12 W of platen power. To create undercuts on the bottom roots of the Si pillars, additional isotropic etching was conducted by using SF_6 gas at a flow rate of 85 sccm, 450 W of RF plasma power, and 30 W of platen power. To remove the passivation layer and photoresist, the specimen underwent two treatments. The first was oxygen (O_2) plasma treatment, which involved using a flow rate of 20 sccm, a power of 150 W, a pressure of 50 mTorr, and a duration of 15 min. The second treatment was piranha solution treatment, which consisted of immersing the specimen in a mixture of 75% H_2SO_4 and 25% H_2O_2. To reduce the size of the Si pillars, the specimen was immersed in a 15 wt % potassium hydroxide (KOH, Fisher Scientific) solution at 25 °C. To create pores on the surface at the nanoscale, metal-assisted chemical etching (MACE) process was employed, which involved immersing the specimen in an etching solution made up of 20 mM Ag nitrate ($AgNO_3$, Sigma-Aldrich) and 49% hydrofluoric (HF) solution (J. T. Baker Inc.).[29,30] After the MACE process, any Ag residues on the surface were removed by immersing the specimen in an Ag etchant solution (TFS, KI−I2 complex liquid, Transene Inc.) for 1 min. Finally, thin films of Ti/Au (3/50 nm) were sputtered over the surface.

Transfer Printing of Si Needles onto PDMS. To initiate the process, an uncured PDMS solution (Sylgard 184) in a 10:1 weight ratio of the base polymer and curing agent was spin-cast at 1500 rpm for 5 min onto a precured PDMS substrate. The PDMS solution was partially cured at room temperature for 3 min to serve as an adhesive layer. The Au-deposited Si needles were then positioned upside down on the PDMS adhesive. A subsequent annealing process was conducted on a hot plate at 130 °C for 10 min to complete the polymerization of the PDMS adhesive and ensure the physical bonding of the Si needles to the PDMS substrate. To release the Si needles from the Si wafer, the entire specimen was immersed in a solvent such as hexane (20 mL; Fisher Scientific). The solvent caused the PDMS substrate to swell, leading to the controlled cracking of the bottom undercuts of the Si needles where mechanical stress can be concentrated during the swelling process.[27] Finally, the resulting specimen was washed with deionized (DI) water and dried in a convection oven at 70 °C for 1 h to remove any remaining solvent, enabling the PDMS to recover to its original size.

Synthesis of Au−Ag Nanowires. The Ag nanowires were synthesized using a conventional hydrothermal method.[68] First, an aqueous solution of Ag nitrate (0.02 M, 15 mL) and an aqueous solution of D+glucose (0.12 g, 5 mL) were mixed while stirring at 300 rpm for 10 min at room temperature. Next, after dissolving 1 g of poly(vinylpyrrolidone) in 5 mL of DI water at 70 °C, the solution was added to the mixture and stirred for 20 min at room temperature. Subsequently, an aqueous solution of sodium chloride (NaCl, 0.04 M, 15 mL) was added dropwise while continuously stirring until completely dissolved. This hydrosol mixture was placed in a 50 mL Teflon-lined stainless-steel autoclave and heated in a dry oven at 160 °C for 22 h. Following the hydrothermal synthesis process, the autoclave was air-cooled to room temperature. The Ag nanowires were washed by centrifugation at 3,000 rpm for 10 min using acetone and ethanol and then thoroughly air-dried. Subsequently, the Ag nanowires were coated with Au using a galvanic-free deposition method, in order not only to prevent oxidation of the Ag but also to enhance electrical conductivity and biocompatibility.[33] Details of this method are as follows: First, 100 mg of the Ag nanowires were mixed in a solution containing 320 mL of DI water, 70 mL of 5 wt % polyvinylpyrrolidone (PVP), 14 mL of 0.5 M sodium hydroxide (NaOH), 14 mL of 0.5 M L-ascorbic acid (L-AA), and 3.5 mL of 0.1 M sodium sulfite (Na_2SO_3). Separately, an Au solution was prepared by mixing 1.4 mL of 0.25 M hydrogen tetrachloroaurate (III) hydrate ($HAuCl_4{\cdot}xH_2O$), 8.4 mL of 0.2 M sodium hydroxide (NaOH), 105 mL of 0.01 M Na_2SO_3, and 165 mL of DI water, then left undisturbed for 12 h. These two solutions were then combined to initiate a reaction to form an Au layer over the surface of the Ag nanowires, and the mixture was left at room temperature for 2 h. The resulting Au−Ag nanowires were washed multiple times through centrifugation at 3,000 rpm for 10 min with acetone and ethanol. The Au−Ag nanowires were then dispersed and stored in ethanol for spraying.

Assembly of the Transparent Intracellular Sensing Platform. The PDMS substrate featuring the Au−Si needles was cut into a size of 2 mm × 2 mm and subsequently bonded to a polyethylene terephthalate (PET) film. This specimen was treated with (3-Aminopropyl)triethoxysilane (APTES) to improve adhesion on the surface and then sprayed with the Au−Ag nanowires multiple times, up to 30 times, using an airbrush (Master Airbrush). A shadow mask, constructed from polyimide tape, was utilized during the spraying process to delineate the conduction path leading to a connection pad; however, no additional protective mask was employed, ensuring that the Au−Si needles remained uncovered and unaffected. The mechanical and electrical connections between the Au−Ag nanowires were reinforced through a chemical welding process. Specifically, the Au−Ag nanowires underwent oxidation via oxygen (O_2) plasma treatment at 90 W for 5 min and were then placed in a sample tray containing a hydrazine hydrate vapor as a reducing agent for 10 min. After the welding process, the shadow mask was removed, and the Au−Ag nanowires were thermally annealed at 90 °C for 1 h. To

https://doi.org/10.1021/acsnano.3c07527
ACS Nano 2023, 17, 25014−25026

passivate the Au−Ag nanowires, a PDMS solution diluted in a thinner (Smooth-On, NOVOCS Gloss Silicone Solvent) at a 1:10 weight ratio was spin-cast over the surface at 300 rpm for 5 min. A RIE process was performed to expose the tips of the Au−Si needles using a 3:1 mixture of O_2 and tetrafluoromethane (CF_4) gases at 200 W and 45 mTorr for 5 min. Finally, a culture well with a diameter of 16.5 mm was attached for the cell culture.

Finite Element Analysis (FEA). The FEA was performed using a commercial software package (ABAQUS) to analyze the deformation of single Au−Si needles under cell contraction. The elastic properties of the constituent materials were considered, including 112.4 GPa and 0.27 for the Au−Si needles and 2 MPa and 0.45 for the PDMS substrate. The Au−Ag nanowire network layer was not included in the FEA due to its location from the surface, its thinness compared to the passivation PDMS layer, and its low density, which ensures a transmittance of over 80%. A tie constraint option was applied to the surface of the PDMS substrate where the Au−Si needles were interconnected to ensure model integrity. A contraction force of 5 μN, applied to a node on the top surface of the Au−Si needles and parallel to the top surface of the PDMS substrate, was used in the analysis.[69,70] Lateral displacement and Encastre boundary conditions were applied to the side and bottom surfaces of the PDMS substrate, respectively.

Optical Transmittance Measurements. The optical transmittance of specimens was measured at wavelengths of 300 to 800 nm using a UV−visible spectrophotometer (Lambda950, PerkinElmer).

Electrochemical Impedance Spectroscopy. Electrochemical impedance spectroscopy was performed with PBS and Ag/AgCl reference electrodes by using a potentiostat (SP-200, Biologic). The specimens were filled with PBS and incubated at 37 °C with 5% CO_2 for 28 days, during which impedance at 1 kHz was measured every 7 days.

Cell Viability Assay. The Au−Si needles were cultured with HL-1 cells and incubated at 37 °C with 5% CO_2 for 3 days. A 3-(4,5-dimethylthiazol-2-yl)-2,5-diphenyltetrazolium bromide (Millipore Sigma) reagent was added at each day and incubated for 3 h. Following the removal of the cell medium, the cells were lysed with dimethyl sulfoxide (Thermo Fisher Scientific), and the absorbance of each well was measured at 575 nm by using a microplate reader (Synergy NEO, BioTek). The cell viability was calculated by normalizing the data, with control values set as 100%, and each group consisted of $n = 5$.

HL-1 Cell Culture. Each specimen was subjected to 10 min of O_2 plasma cleaning and coated with a 5 μg mL^{-1} fibronectin solution in 0.02% w/w gelatin. After incubating at 37 °C with 5% CO_2 for 1 h, HL-1 cells (Millipore Sigma) were seeded at a density of 12.5×10^4 per well in Claycomb medium (supplemented with 10% HL-1 qualified fetal bovine serum, 0.1 mM norepinephrine, 2 mM L-glutamine, and 100 U mL^{-1} of penicillin and 100 U mL^{-1} of streptomycin, Millipore Sigma) and incubated at 37 °C with 5% CO_2. The medium was changed daily.

Immunofluorescent Staining and Imaging. Immunofluorescent staining and imaging were conducted on the Au−Si needles using Immunoglobulin G 488 (IgG 488, Invitrogen) to facilitate fluorescent visualization. In Figures 3E and 4F, two distinct loading methods, namely physical and chemical loading, were employed for IgG 488 on the Au−Si needles. For physical loading, a droplet of IgG 488 was applied to the needles and allowed to interact for 10 min at room temperature. Subsequently, the needles were rinsed with ethanol and subjected to N_2 gas drying. For chemical loading, the needles were treated with 100 μL of 3-triethoxysilylpropyl succinic anhydride (TESPSA; Gelest) at room temperature for 10 min to functionalize the surface with silane before being washed with ethanol. Specifically, 30 μg of IgG 488 was prepared by mixing 50 μL of IgG 488, with a concentration of 600 μg mL−1, with 950 μL of PBS. The Au−Si needles were treated with this solution for 30 min at room temperature, followed by a rinse with ethanol.[29] Live staining on HL-1 cells was performed using CellMaskTM (Invitrogen) for cell membrane visualization and Hoechst (Invitrogen) for nucleus staining. An inverted confocal microscope (LSM 880, Zeiss) was employed to capture 3D images of the interface between the cells and the Au−Si needles.

Electrophysiology Recording. After spontaneous beating was observed and HL-1 cells reached confluency, the Au−Si needles of our sensing platform were mechanically inserted into the cells by centrifuging them at 500 rpm for 1 min. For the 3D-engineered cardiovascular tissues, our sensing platform was placed on top of the differentiated organoid and allowed to rest for 5 min. Our sensing platform was then connected to a PowerLab data acquisition system and BioAmps amplifier (AD Instruments) that was recorded at a sampling rate of 10 kHz and a low-pass filter of 3 kHz. An Ag/AgCl electrode (PINE Research) was used as the reference electrode. Electroporation was carried out using a signal generator (Keithley 3390, Keithley), which applied biphasic square pulses with a period of 400 μs and an amplitude of 4 V for 1 s. The position of the electrode, specifically whether the needle tip is inside or outside the cell membrane, can be determined by the amplitude's noise level and peak sign. A shift of the peak from negative to positive after electroporation indicates that the electrode has penetrated the intracellular cytoplasm, producing a signal with an amplitude more than ten times higher and significantly reduced noise. Additionally, the cell membrane recovers after electroporation, allowing for repeated procedures and prolonged recording.[9,10] During electroporation and 30 s afterward, the recording system was disconnected to avoid amplifier saturation.

Calcium Flux Imaging. For HL-1 cells, Tyrode's solution containing 5 μM Fluo-8 (AAT Bioquest) was used to substitute the Claycomb medium, which was then incubated at 37 °C with 5% CO_2 for 1 h. Subsequently, the solution was rinsed and replaced with Tyrode's solution, and the specimen was observed using an inverted microscope (Axio Observer Z1/7, Zeiss) at excitation and emission wavelengths of 488 and 515 nm, respectively. The 3D-engineered cardiovascular tissues were incubated in a medium with a calcium indicator from the Fluo-4 Direct Calcium Assay Kit (Invitrogen) for 1 h, and imaging was performed at room temperature using the time series mode of a laser scanning confocal microscope (LSM 710, Zeiss). The signal intensity of pixels in the green channel of the acquired images was averaged, and the calcium transient amplitude ($\Delta F/F_0$) was calculated as the difference between the peak and baseline calcium fluorescence (ΔF) divided by the baseline fluorescence level (F_0). Images were collected and subsequently analyzed using ZEN (Zeiss) and ImageJ software.

Drug Assay. To prepare the drug solution, Nifedipine (Abcam) was dissolved in dimethyl sulfoxide (DMSO, Fisher Scientific). The resulting solution was diluted in Claycomb medium to achieve a final concentration of 100 nM Nifedipine and 0.01% DMSO. Action potentials were initially recorded without drugs as a reference. The cells were then allowed to recover by incubating at 37 °C with 5% CO_2 for 1 h. Subsequently, Nifedipine was added to the culture medium and incubated for 10 min at 37 °C with 5% CO_2. This was followed by mechanoporation and electroporation, after which action potentials were recorded.

3D Cardiovascular Tissue Formation. The organoids were formed on collagen-polyethylene glycol (PEG) hydrogel formulated with methods described previously.[71,72] In brief, hydrogels were formed by *in situ* cross-linking of bovine type I collagen (3 mg mL^{-1}, Advanced Biomatrix) in an equal volume of serum-free ESC medium. To initiate gel formation, reconstitution solution (0.26 M sodium hydrogen carbonate, 0.2 M HEPES, and 0.04 M sodium hydroxide) was added, and the solution was then incubated at 37 °C for at least 30 min. Mouse ESCs (ATCC) cultured with high glucose Dulbecco's Modified Eagle Medium (Corning) including supplements (15% ESC certified fetal bovine serum (FBS), 0.1 mM 2-mercaptoethanol, 1× MEM nonessential amino acid, 1000 U ml^{-1} mouse leukemia inhibitory factor, and 1% penicillin-streptomycin (PS) were assembled into EBs through hanging drop culture (2,000 cells per 20 μL media drops) for 3 days. The resulting EBs were then placed on collagen hydrogels and cultured with a cardiomyocyte differentiation kit (Gibco) for 14 days to engineer the 3D cardiovascular tissue model.

3D Cardiovascular Tissue Characterizations. On Day 14, immunofluorescence staining was carried out on organoids. The

https://doi.org/10.1021/acsnano.3c07527
ACS Nano 2023, 17, 25014−25026

differentiated EBs underwent sequential fixation (using a 4% paraformaldehyde solution at room temperature for 15 min), permeabilization (with a 0.1% Triton X-100 solution for 10 min), and blocking (with 5% FBS and 0.1% Tween-20 for 1 h). Primary antibodies to cTnT and α-actinin were then applied to the differentiated EBs, which were incubated at 4 °C overnight. A 1:100 dilution of the antibodies in a blocking buffer was used for this purpose. Subsequently, cells were exposed to secondary antibody antimouse conjugated Alexa 488 or 555 (1:100 dilution) for 1 h at room temperature. Nucleus staining was performed with DAPI (1:1000 dilution), and immune-stained images were captured using a confocal microscope (LSM 700, Zeiss). The gene expression levels of differentiated EBs were evaluated via real-time PCR. After 14 days of differentiation, the genes encoding cardiomyogenic markers and calcium handling markers were analyzed. mRNA purification was performed using an RNeasy Mini Kit (Qiagen). A Nanodrop spectrophotometer (Thermo Scientific) was employed to quantify the isolated mRNA. Subsequently, cDNA was synthesized in a thermal cycler (Bio-Rad, MyCycler) by combining mRNA (1 mg) and an iScript cDNA synthesis kit in a 20 μL reaction volume, following the instructions of the manufacturer. The synthesized cDNA was utilized in real-time PCR reactions executed with SYBR Premix (Bio-Rad, iTaq Universal SYBR Green Supermix). The reactions, consisting of 40 cycles, were conducted in an RT PCR machine (Roche, Lightcycler 480). Each cycle included melting at 95 °C for 15 s, followed by annealing and extension at 60 °C for 60 s for each primer pair. The real-time PCR data were analyzed by using the comparative threshold cycle method. The relative expression of each gene, in comparison to the expression level of GAPDH, was calculated and then normalized to the undifferentiated EBs. Each gene amplification assay was carried out in triplicate. Melting curves were generated, and negative controls were scrutinized to ensure that primer dimers did not affect the results.

Statistical Analyses. All data are presented as mean ± standard deviation. For Figures 2F, S10, and S11, a one-way analysis of variance (ANOVA) accompanied by the Tukey test was utilized, with a significance level set at 0.005.

ASSOCIATED CONTENT

Data Availability Statement

The data that support the plots and other findings of this study are available from the corresponding authors upon reasonable request.

Supporting Information

The Supporting Information is available free of charge at https://pubs.acs.org/doi/10.1021/acsnano.3c07527.

Detailed fabrication methods and analysis results of the proposed intracellular recording platform (PDF)

Movie S1: Finite Element Analysis (FEA) Results - Showcasing detailed strain and stress distributions in a silicon needle when applied to a PDMS surface (MOV)

Movie S2: Growth and Development of HL-1 Cells - Capturing their 3-5 day journey to confluency, this segment illustrates their natural, spontaneous beating (MP4)

Movie S3: Intricate Calcium Flux in HL-1 Cells - Observing the microscopic world of HL-1 cells, focusing on the changes in calcium flux during a single action potential (MP4)

Movie S4: Fluorescence Calcium Flux in Cardiovascular Organoids - Exploring the dynamic fluorescence calcium flux within cells derived from cardiovascular organoids, providing a unique perspective on cellular processes (MP4)

AUTHOR INFORMATION

Corresponding Authors

Dong Rip Kim − *School of Mechanical Engineering, Hanyang University, Seoul 04763, Republic of Korea;* orcid.org/0000-0001-6398-9483; Email: dongrip@hanyang.ac.kr

Hyunjoon Kong − *Department of Chemical and Biomolecular Engineering, University of Illinois at Urbana−Champaign, Urbana, Illinois 61801, United States; Carl R. Woese Institute for Genomic Biology, University of Illinois at Urbana−Champaign, Urbana, Illinois 61801, United States;* orcid.org/0000-0003-4680-2968; Email: hjkong06@illinois.edu

Chi Hwan Lee − *School of Mechanical Engineering, Weldon School of Biomedical Engineering, and Department of Materials Engineering, Purdue University, West Lafayette, Indiana 47907, United States;* orcid.org/0000-0002-4868-7054; Email: lee2270@purdue.edu

Authors

Woohyun Park − *School of Mechanical Engineering, Purdue University, West Lafayette, Indiana 47907, United States;* orcid.org/0000-0002-1799-3104

Eun Mi Kim − *Department of Chemical and Biomolecular Engineering, University of Illinois at Urbana−Champaign, Urbana, Illinois 61801, United States*

Yale Jeon − *School of Mechanical Engineering, Hanyang University, Seoul 04763, Republic of Korea*

Junsang Lee − *School of Mechanical Engineering, Hanyang University, Seoul 04763, Republic of Korea; Weldon School of Biomedical Engineering, Purdue University, West Lafayette, Indiana 47907, United States*

Jonghun Yi − *School of Mechanical Engineering, Hanyang University, Seoul 04763, Republic of Korea*

Jinheon Jeong − *Weldon School of Biomedical Engineering, Purdue University, West Lafayette, Indiana 47907, United States*

Bongjoong Kim − *School of Mechanical Engineering, Purdue University, West Lafayette, Indiana 47907, United States; Department of Mechanical and System Design Engineering, Hongik University, Seoul 04066, Republic of Korea;* orcid.org/0000-0002-9969-6954

Byeong Guk Jeong − *School of Mechanical Engineering, Hanyang University, Seoul 04763, Republic of Korea; Weldon School of Biomedical Engineering, Purdue University, West Lafayette, Indiana 47907, United States*

Complete contact information is available at: https://pubs.acs.org/10.1021/acsnano.3c07527

Author Contributions

▼W.P., E.M.K., Y.J., and J.L. contributed equally to this work. H.K., D.R.K., and C.H.L. conceived the concept; planned the project; and supervised the research. W.P., Y.J., J.L., J.Y., J. J., B.K., B.G.J., D.R.K., and C.H.L. conducted the experiments and data analysis on the platform development and HL-1 experiments. E.M.K. and H.K. designed, fabricated, and characterized the organoid studies. W.P., E.M.K., Y.J., J.L., D.R.K., H.K., and C.H.L. wrote the manuscript. All authors commented on the paper.

Notes

The authors declare no competing financial interest.

https://doi.org/10.1021/acsnano.3c07527
ACS Nano 2023, 17, 25014−25026

ACKNOWLEDGMENTS

C.H.L. and H.K. acknowledge funding support from National Science Foundation (NSF) Division of Chemical, Bioengineering, Environmental, and Transport Systems (CBET) (2032529). C.H.L. acknowledges the funding support from National Institutes of Health (NIH) National Eye Institute (NEI) (R01EY033000) and the Leslie A. Geddes Endowment at Purdue University. D.R.K. acknowledges the funding support from the Basic Science Research Program (NRF-2021R1A2C1011418) and the Nano-Material Technology Development Program (NRF-2022M3H4A1A02046445) through the National Research Foundation of Korea (NRF) funded by the Ministry of Science and ICT of Korea. B.G.J. acknowledges the funding support from the Ministry of Trade, Industry, and Energy (MOTIE) in Korea, under the Human Resource Development Program for Industrial Innovation (Global) (P0017306; Global Human Resource Development for Innovative Design in Robot and Engineering) supervised by the Korea Institute for Advancement of Technology (KIAT).

REFERENCES

(1) Abbott, J.; Ye, T.; Krenek, K.; Gertner, R. S.; Ban, S.; Kim, Y.; Qin, L.; Wu, W.; Park, H.; Ham, D. A Nanoelectrode Array for Obtaining Intracellular Recordings from Thousands of Connected Neurons. *Nat. Biomed. Eng.* **2020**, *4* (2), 232−241.

(2) Obaid, A.; Hanna, M. E.; Wu, Y. W.; Kollo, M.; Racz, R.; Angle, M. R.; Müller, J.; Brackbill, N.; Wray, W.; Franke, F.; Chichilnisky, E. J.; Hierlemann, A.; Ding, J. B.; Schaefer, A. T.; Melosh, N. A. Massively Parallel Microwire Arrays Integrated with CMOS Chips for Neural Recording. *Sci. Adv.* **2020**, *6* (12), No. eaay2789.

(3) Jiang, Y.; Tian, B. Inorganic Semiconductor Biointerfaces. *Nat. Rev. Mater.* **2018**, *3* (12), 473−490.

(4) Fang, Y.; Yang, X.; Lin, Y.; Shi, J.; Prominski, A.; Clayton, C.; Ostroff, E.; Tian, B. Dissecting Biological and Synthetic Soft-Hard Interfaces for Tissue-Like Systems. *Chem. Rev.* **2022**, *122* (5), 5233−5276.

(5) Frank, J. A.; Antonini, M.-J.; Anikeeva, P. Next-Generation Interfaces for Studying Neural Function. *Nat. Biotechnol.* **2019**, *37* (9), 1013−1023.

(6) Hong, G.; Lieber, C. M. Novel Electrode Technologies for Neural Recordings. *Nat. Rev. Neurosci.* **2019**, *20* (6), 330−345.

(7) Zhang, M.; Tang, Z.; Liu, X.; Van der Spiegel, J. Electronic Neural Interfaces. *Nat. Electron.* **2020**, *3* (4), 191−200.

(8) Kruskal, P. B.; Jiang, Z.; Gao, T.; Lieber, C. M. Beyond the Patch Clamp: Nanotechnologies for Intracellular Recording. *Neuron* **2015**, *86* (1), 21−24.

(9) Xie, C.; Lin, Z.; Hanson, L.; Cui, Y.; Cui, B. Intracellular Recording of Action Potentials by Nanopillar Electroporation. *Nat. Nanotechnol.* **2012**, *7* (3), 185−190.

(10) Lin, Z. C.; Xie, C.; Osakada, Y.; Cui, Y.; Cui, B. Iridium Oxide Nanotube Electrodes for Sensitive and Prolonged Intracellular Measurement of Action Potentials. *Nat. Commun.* **2014**, *5* (1), No. 3206.

(11) Liu, R.; Lee, J.; Tchoe, Y.; Pre, D.; Bourhis, A. M.; D'Antonio-Chronowska, A.; Robin, G.; Lee, S. H.; Ro, Y. G.; Vatsyayan, R.; Tonsfeldt, K. J.; Hossain, L. A.; Phipps, M. L.; Yoo, J.; Nogan, J.; Martinez, J. S.; Frazer, K. A.; Bang, A. G.; Dayeh, S. A. Ultra-Sharp Nanowire Arrays Natively Permeate, Record, and Stimulate Intracellular Activity in Neuronal and Cardiac Networks. *Adv. Funct. Mater.* **2022**, *32*, 2108378.

(12) Cao, Y.; Hjort, M.; Chen, H.; Birey, F.; Leal-Ortiz, S. A.; Han, C. M.; Santiago, J. G.; Paşca, S. P.; Wu, J. C.; Melosh, N. A. Nondestructive Nanostraw Intracellular Sampling for Longitudinal Cell Monitoring. *Proc. Natl. Acad. Sci. U. S. A.* **2017**, *114* (10), E1866−E1874.

(13) Wen, R.; Zhang, A. H.; Liu, D.; Feng, J.; Yang, J.; Xia, D.; Wang, J.; Li, C.; Zhang, T.; Hu, N.; Hang, T.; He, G.; Xie, X. Intracellular Delivery and Sensing System Based on Electroplated Conductive Nanostraw Arrays. *ACS Appl. Mater. Interfaces* **2019**, *11*, 43936−43948.

(14) Liu, R.; Chen, R.; Elthakeb, A. T.; Lee, S. H.; Hinckley, S.; Khraiche, M. L.; Scott, J.; Pre, D.; Hwang, Y.; Tanaka, A.; Ro, Y. G.; Matsushita, A. K.; Dai, X.; Soci, C.; Biesmans, S.; James, A.; Nogan, J.; Jungjohann, K. L.; Pete, D. V.; Webb, D. B.; Zou, Y.; Bang, A. G.; Dayeh, S. A. High Density Individually Addressable Nanowire Arrays Record Intracellular Activity from Primary Rodent and Human Stem Cell Derived Neurons. *Nano Lett.* **2017**, *17* (5), 2757−2764.

(15) Robinson, J. T.; Jorgolli, M.; Shalek, A. K.; Yoon, M. H.; Gertner, R. S.; Park, H. Vertical Nanowire Electrode Arrays as a Scalable Platform for Intracellular Interfacing to Neuronal Circuits. *Nat. Nanotechnol.* **2012**, *7* (3), 180−184.

(16) Shalek, A. K.; Robinson, J. T.; Karp, E. S.; Lee, J. S.; Ahn, D.-R.; Yoon, M.-H.; Sutton, A.; Jorgolli, M.; Gertner, R. S.; Gujral, T. S.; MacBeath, G.; Yang, E. G.; Park, H. Vertical Silicon Nanowires as a Universal Platform for Delivering Biomolecules into Living Cells. *Proc. Natl. Acad. Sci. U. S. A.* **2010**, *107* (5), 1870−1875.

(17) Shi, J.; Sun, C.; Liang, E.; Tian, B. Semiconductor Nanowire-Based Cellular and Subcellular Interfaces. *Adv. Funct. Mater.* **2022**, *32* (11), No. 2107997.

(18) Lee, Y. V.; Wu, D.; Fang, Y.; Peng, Y.; Tian, B. Tracking Longitudinal Rotation of Silicon Nanowires for Biointerfaces. *Nano Lett.* **2020**, *20* (5), 3852−3857.

(19) Tian, B.; Lieber, C. M. Nanowired Bioelectric Interfaces. *Chem. Rev.* **2019**, *119* (15), 9136−9152.

(20) Fine, D.; Grattoni, A.; Goodall, R.; Bansal, S. S.; Chiappini, C.; Hosali, S.; van de Ven, A. L.; Srinivasan, S.; Liu, X.; Godin, B.; Brousseau, L.; Yazdi, I. K.; Fernandez-Moure, J.; Tasciotti, E.; Wu, H. J.; Hu, Y.; Klemm, S.; Ferrari, M. Silicon Micro- and Nanofabrication for Medicine. *Adv. Healthc. Mater.* **2013**, *2* (5), 632−666.

(21) Betzig, E.; Patterson, G. H.; Sougrat, R.; Lindwasser, O. W.; Olenych, S.; Bonifacino, J. S.; Davidson, M. W.; Lippincott-Schwartz, J.; Hess, H. F. Imaging Intracellular Fluorescent Proteins at Nanometer Resolution. *Science* **2006**, *313* (5793), 1642−1645.

(22) Acharya, A.; Nemade, H.; Prasad, K. R.; Khan, K.; Hescheler, J.; Blackburn, N.; Hemmersbach, R.; Papadopoulos, S.; Sachinidis, A. Live-Cell Imaging of the Contractile Velocity and Transient Intracellular Ca2+ Fluctuations in Human Stem Cell-Derived Cardiomyocytes. *Cells* **2022**, *11* (8), 1280.

(23) Lu, W.; Hu, R.; Tong, X.; Yu, D.; Zhao, Q. Electro-Optical Detection of Single Molecules Based on Solid-State Nanopores. *Small Struct* **2020**, *1* (1), No. 2000003.

(24) Marvin, J. S.; Borghuis, B. G.; Tian, L.; Cichon, J.; Harnett, M. T.; Akerboom, J.; Gordus, A.; Renninger, S. L.; Chen, T. W.; Bargmann, C. I.; Orger, M. B.; Schreiter, E. R.; Demb, J. B.; Gan, W. B.; Hires, S. A.; Looger, L. L. An Optimized Fluorescent Probe for Visualizing Glutamate Neurotransmission. *Nat. Methods* **2013**, *10* (2), 162−170.

(25) Qiang, Y.; Artoni, P.; Seo, K. J.; Culaclii, S.; Hogan, V.; Zhao, X.; Zhong, Y.; Han, X.; Wang, P. M.; Lo, Y. K.; Li, Y.; Patel, H. A.; Huang, Y.; Sambangi, A.; Chu, J. S. V.; Liu, W.; Fagiolini, M.; Fang, H. Transparent Arrays of Bilayer-Nanomesh Microelectrodes for Simultaneous Electrophysiology and Two-Photon Imaging in the Brain. *Sci. Adv.* **2018**, *4* (9), eaat0626.

(26) Thunemann, M.; Lu, Y.; Liu, X.; Kılıç, K.; Desjardins, M.; Vandenberghe, M.; Sadegh, S.; Saisan, P. A.; Cheng, Q.; Weldy, K. L.; Lyu, H.; Djurovic, S.; Andreassen, O. A.; Dale, A. M.; Devor, A.; Kuzum, D. Deep 2-Photon Imaging and Artifact-Free Optogenetics through Transparent Graphene Microelectrode Arrays. *Nat. Commun.* **2018**, *9* (1), No. 2035.

(27) Park, D.-W.; Brodnick, S. K.; Ness, J. P.; Atry, F.; Krugner-Higby, L.; Sandberg, A.; Mikael, S.; Richner, T. J.; Novello, J.; Kim, H.; Baek, D.-H.; Bong, J.; Frye, S. T.; Thongpang, S.; Swanson, K. I.; Lake, W.; Pashaie, R.; Williams, J. C.; Ma, Z. Fabrication and Utility of a Transparent Graphene Neural Electrode Array for Electro-

https://doi.org/10.1021/acsnano.3c07527
ACS Nano 2023, 17, 25014−25026

physiology, in Vivo Imaging, and Optogenetics. *Nat. Protoc.* **2016**, *11* (11), 2201−2222.
(28) Nie, B.; Huang, R.; Yao, T.; Zhang, Y.; Miao, Y.; Liu, C.; Liu, J.; Chen, X. Textile-Based Wireless Pressure Sensor Array for Human-Interactive Sensing. *Adv. Funct Mater.* **2019**, *29* (22), 1808786.
(29) Obaid, S. N.; Quirion, N.; Torres Balansag, J. D.; Daza, N.; Shi, X.; Chen, Z.; Lu, L. Design and Fabrication of a Flexible Opto-Electric Biointerface for Multimodal Optical Fluorescence and Electrical Recording. *ACS Appl. Electron Mater.* **2023**, *5* (3), 1688−1696.
(30) Susloparova, A.; Halliez, S.; Begard, S.; Colin, M.; Buee, L.; Pecqueur, S.; Alibart, F.; Thomy, V.; Arscott, S.; Pallecchi, E.; Coffinier, Y. Low Impedance and Highly Transparent Microelectrode Arrays (MEA) for in Vitro Neuron Electrical Activity Probing. *Sens Actuators B Chem.* **2021**, *327*, No. 128895.
(31) Khraiche, M. L.; El Hassan, R. Advances in Three-Dimensional Nanostructures for Intracellular Recordings from Electrogenic Cells. *Journal of Science: Advanced Materials and Devices* **2020**, *5*, 279−294.
(32) Kim, H.; Jang, H.; Kim, B.; Kim, M. K.; Wie, D. S.; Lee, H. S.; Kim, D. R.; Lee, C. H. Flexible Elastomer Patch with Vertical Silicon Nanoneedles for Intracellular and Intratissue Nanoinjection of Biomolecules. *Sci. Adv.* **2018**, *4* (11), No. eaau6972.
(33) Shkumatov, A.; Baek, K.; Kong, H. Matrix Rigidity-Modulated Cardiovascular Organoid Formation from Embryoid Bodies. *PLoS One* **2014**, *9* (4), e94764.
(34) Park, W.; Nguyen, V. P.; Jeon, Y.; Kim, B.; Li, Y.; Yi, J.; Kim, H.; Leem, J. W.; Kim, Y. L.; Kim, D. R.; Paulus, Y. M.; Lee, C. H. Biodegradable Silicon Nanoneedles for Ocular Drug Delivery. *Sci. Adv.* **2022**, *8* (13), 1772.
(35) Kim, H.; Lee, H. S.; Jeon, Y.; Park, W.; Zhang, Y.; Kim, B.; Jang, H.; Xu, B.; Yeo, Y.; Kim, D. R.; Lee, C. H. Bioresorbable, Miniaturized Porous Silicon Needles on a Flexible Water-Soluble Backing for Unobtrusive, Sustained Delivery of Chemotherapy. *ACS Nano* **2020**, *14* (6), 7227−7236.
(36) Rodríguez-Manzo, J. A.; Puster, M.; Nicolaï, A.; Meunier, V.; Drndić, M. DNA Translocation in Nanometer Thick Silicon Nanopores. *ACS Nano* **2015**, *9* (6), 6555−6564.
(37) Xie, P.; Xiong, Q.; Fang, Y.; Qing, Q.; Lieber, C. M. Local Electrical Potential Detection of DNA by Nanowire−Nanopore Sensors. *Nat. Nanotechnol.* **2012**, *7* (2), 119−125.
(38) Choi, S.; Han, S. I.; Jung, D.; Hwang, H. J.; Lim, C.; Bae, S.; Park, O. K.; Tschabrunn, C. M.; Lee, M.; Bae, S. Y.; Yu, J. W.; Ryu, J. H.; Lee, S. W.; Park, K.; Kang, P. M.; Lee, W. B.; Nezafat, R.; Hyeon, T.; Kim, D. H. Highly Conductive, Stretchable and Biocompatible Ag−Au Core−Sheath Nanowire Composite for Wearable and Implantable Bioelectronics. *Nat. Nanotechnol.* **2018**, *13* (11), 1048−1056.
(39) Lee, J.; Lee, I.; Kim, T. S.; Lee, J. Y. Efficient Welding of Silver Nanowire Networks without Post-Processing. *Small* **2013**, *9* (17), 2887−2894.
(40) Ahn, J.; Seo, J. W.; Kim, J. Y.; Lee, J.; Cho, C.; Kang, J.; Choi, S. Y.; Lee, J. Y. Self-Supplied Nano-Fusing and Transferring Metal Nanostructures via Surface Oxide Reduction. *ACS Appl. Mater. Interfaces* **2016**, *8* (2), 1112−1119.
(41) Chen, Z.; Nguyen, K.; Kowalik, G.; Shi, X.; Tian, J.; Doshi, M.; Alber, B. R.; Guan, X.; Liu, X.; Ning, X.; Kay, M. W.; Lu, L. Transparent and Stretchable Au−Ag Nanowire Recording Microelectrode Arrays. *Adv. Mater. Technol.* **2023**, *8* (10), No. 2201716.
(42) Park, S.; Nguyen, D.-V.; Kang, L. Immobilized Nanoneedle-like Structures for Intracellular Delivery, Biosensing and Cellular Surgery. *Nanomedicine* **2021**, *16* (4), 335−349.
(43) Penedo, M.; Shirokawa, T.; Alam, M. S.; Miyazawa, K.; Ichikawa, T.; Okano, N.; Furusho, H.; Nakamura, C.; Fukuma, T. Cell Penetration Efficiency Analysis of Different Atomic Force Microscopy Nanoneedles into Living Cells. *Sci. Rep* **2021**, *11* (1), No. 7756.
(44) Coffey, J. W.; van der Burg, N. M. D.; Rananakomol, T.; Ng, H.-I.; Fernando, G. J. P.; Kendall, M. A. F. An Ultrahigh-Density Microneedle Array for Skin Vaccination: Inducing Epidermal Cell Death by Increasing Microneedle Density Enhances Total IgG and IgG1 Immune Responses. *Adv. Nanobiomed Res.* **2022**, *2* (8), No. 2100151.
(45) Sara, B.; Trine, B.; Hannibal, M. M.; Kristian, A. T.; Nina, B.-M.; Lei, G.; Xiaomei, L.; Florent, B.; Karine, A.; Jesper, N. Tuning InAs Nanowire Density for HEK293 Cell Viability, Adhesion, and Morphology: Perspectives for Nanowire-Based Biosensors. *ACS Appl. Mater. Interfaces* **2013**, *5*, 10510.
(46) Caprettini, V.; Cerea, A.; Melle, G.; Lovato, L.; Capozza, R.; Huang, J.-A.; Tantussi, F.; Dipalo, M.; De Angelis, F. Soft Electroporation for Delivering Molecules into Tightly Adherent Mammalian Cells through 3D Hollow Nanoelectrodes. *Sci. Rep* **2017**, *7* (1), No. 8524.
(47) Kim, J. A.; Aberg, C.; Salvati, A.; Dawson, K. A. Role of Cell Cycle on the Cellular Uptake and Dilution of Nanoparticles in a Cell Population. *Nat. Nanotechnol.* **2012**, *7* (1), 62−68.
(48) Xie, X.; Xu, A. M.; Angle, M. R.; Tayebi, N.; Verma, P.; Melosh, N. A. Mechanical Model of Vertical Nanowire Cell Penetration. *Nano Lett.* **2013**, *13* (12), 6002−6008.
(49) Xu, A. M.; Aalipour, A.; Leal-Ortiz, S.; Mekhdjian, A. H.; Xie, X.; Dunn, A. R.; Garner, C. C.; Melosh, N. A. Quantification of Nanowire Penetration into Living Cells. *Nat. Commun.* **2014**, *5*, No. 3613.
(50) Grienberger, C.; Konnerth, A. Imaging Calcium in Neurons. *Neuron* **2012**, *73* (5), 862−885.
(51) Chen, T. W.; Wardill, T. J.; Sun, Y.; Pulver, S. R.; Renninger, S. L.; Baohan, A.; Schreiter, E. R.; Kerr, R. A.; Orger, M. B.; Jayaraman, V.; Looger, L. L.; Svoboda, K.; Kim, D. S. Ultrasensitive Fluorescent Proteins for Imaging Neuronal Activity. *Nature* **2013**, *499* (7458), 295−300.
(52) Nakai, J.; Ohkura, M.; Imoto, K. A High Signal-to-Noise Ca2+ Probe Composed of a Single Green Fluorescent Protein. *Nat. Biotechnol.* **2001**, *19* (2), 137−141.
(53) Triggle, D. J. Calcium Channel Antagonists: Clinical Uses—Past, Present and Future. *Biochem. Pharmacol.* **2007**, *74* (1), 1−9.
(54) Jan, L. Y.; Jan, Y. N. Voltage-Gated Potassium Channels and the Diversity of Electrical Signalling. *J. Physiol.* **2012**, *590* (11), 2591−2599.
(55) Dipalo, M.; Rastogi, S. K.; Matino, L.; Garg, R.; Bliley, J.; Iachetta, G.; Melle, G.; Shrestha, R.; Shen, S.; Santoro, F.; Feinberg, A. W.; Barbaglia, A.; Cohen-Karni, T.; De Angelis, F. Intracellular Action Potential Recordings from Cardiomyocytes by Ultrafast Pulsed Laser Irradiation of Fuzzy Graphene Microelectrodes. *Sci. Adv.* **2021**, *7* (15), No. eabd5175.
(56) Gu, Y.; Wang, C.; Kim, N.; Zhang, J.; Wang, T. M.; Stowe, J.; Nasiri, R.; Li, J.; Zhang, D.; Yang, A.; Hsu, L. H.; Dai, X.; Mu, J.; Liu, Z.; Lin, M.; Li, W.; Wang, C.; Gong, H.; Chen, Y.; Lei, Y.; Hu, H.; Li, Y.; Zhang, L.; Huang, Z.; Zhang, X.; Ahadian, S.; Banik, P.; Zhang, L.; Jiang, X.; Burke, P. J.; Khademhosseini, A.; McCulloch, A. D.; Xu, S. Three-Dimensional Transistor Arrays for Intra- and Inter-Cellular Recording. *Nat. Nanotechnol.* **2022**, *17*, 292.
(57) Lancaster, M. A.; Knoblich, J. A. Organogenesis in a Dish: Modeling Development and Disease Using Organoid Technologies. *Science* **2014**, *345* (6194), 1247125.
(58) Sullivan, K. M.; Ko, E.; Kim, E. M.; Ballance, W. C.; Ito, J. D.; Chalifoux, M.; Kim, Y. J.; Bashir, R.; Kong, H. Extracellular Microenvironmental Control for Organoid Assembly. *Tissue Eng. Part B Rev.* **2022**, *28* (6), 1209−1222.
(59) Clevers, H. Modeling Development and Disease with Organoids. *Cell* **2016**, *165* (7), 1586−1597.
(60) Takebe, T.; Sekine, K.; Enomura, M.; Koike, H.; Kimura, M.; Ogaeri, T.; Zhang, R. R.; Ueno, Y.; Zheng, Y. W.; Koike, N.; Aoyama, S.; Adachi, Y.; Taniguchi, H. Vascularized and Functional Human Liver from an IPSC-Derived Organ Bud Transplant. *Nature* **2013**, *499* (7459), 481−484.
(61) Lancaster, M. A.; Renner, M.; Martin, C. A.; Wenzel, D.; Bicknell, L. S.; Hurles, M. E.; Homfray, T.; Penninger, J. M.; Jackson, A. P.; Knoblich, J. A. Cerebral Organoids Model Human Brain Development and Microcephaly. *Nature* **2013**, *501* (7467), 373−379.

https://doi.org/10.1021/acsnano.3c07527
ACS Nano 2023, 17, 25014−25026

(62) Fatehullah, A.; Tan, S. H.; Barker, N. Organoids as an in Vitro Model of Human Development and Disease. *Nat. Cell Biol.* **2016**, *18* (3), 246−254.
(63) Drost, J.; Clevers, H. Organoids in Cancer Research. *Nat. Rev. Cancer* **2018**, *18* (7), 407−418.
(64) Ryu, H.; Park, Y.; Luan, H.; Dalgin, G.; Jeffris, K.; Yoon, H. J.; Chung, T. S.; Kim, J. U.; Kwak, S. S.; Lee, G.; Jeong, H.; Kim, J.; Bai, W.; Kim, J.; Jung, Y. H.; Tryba, A. K.; Song, J. W.; Huang, Y.; Philipson, L. H.; Finan, J. D.; Rogers, J. A. Transparent, Compliant 3D Mesostructures for Precise Evaluation of Mechanical Characteristics of Organoids. *Adv. Mater.* **2021**, *33* (25), 1−9.
(65) Li, Q.; Nan, K.; Le Floch, P.; Lin, Z.; Sheng, H.; Blum, T. S.; Liu, J. Cyborg Organoids: Implantation of Nanoelectronics via Organogenesis for Tissue-Wide Electrophysiology. *Nano Lett.* **2019**, *19* (8), 5781−5789.
(66) Zhang, Y. S.; Aleman, J.; Shin, S. R.; Kilic, T.; Kim, D.; Mousavi Shaegh, S. A.; Massa, S.; Riahi, R.; Chae, S.; Hu, N.; Avci, H.; Zhang, W.; Silvestri, A.; Sanati Nezhad, A.; Manbohi, A.; De Ferrari, F.; Polini, A.; Calzone, G.; Shaikh, N.; Alerasool, P.; Budina, E.; Kang, J.; Bhise, N.; Ribas, J.; Pourmand, A.; Skardal, A.; Shupe, T.; Bishop, C. E.; Dokmeci, M. R.; Atala, A.; Khademhosseini, A. Multisensor-Integrated Organs-on-Chips Platform for Automated and Continual in Situ Monitoring of Organoid Behaviors. *Proc. Natl. Acad. Sci. U. S. A.* **2017**, *114* (12), E2293−E2302.
(67) Kim, M.; Hwang, J. C.; Min, S.; Park, Y. G.; Kim, S.; Kim, E.; Seo, H.; Chung, W. G.; Lee, J.; Cho, S. W.; Park, J. U. Multimodal Characterization of Cardiac Organoids Using Integrations of Pressure-Sensitive Transistor Arrays with Three-Dimensional Liquid Metal Electrodes. *Nano Lett.* **2022**, *22* (19), 7892−7901.
(68) Jia, Y.; Chen, C.; Jia, D.; Li, S.; Ji, S.; Ye, C. Silver Nanowire Transparent Conductive Films with High Uniformity Fabricated via a Dynamic Heating Method. *ACS Appl. Mater. Interfaces* **2016**, *8* (15), 9865−9871.
(69) Li, Z.; Song, J.; Mantini, G.; Lu, M. Y.; Fang, H.; Falconi, C.; Chen, L. J.; Wang, Z. L. Quantifying the Traction Force of a Single Cell by Aligned Silicon Nanowire Array. *Nano Lett.* **2009**, *9* (10), 3575−3580.
(70) Zheng, Q.; Peng, M.; Liu, Z.; Li, S.; Han, R.; Ouyang, H.; Fan, Y.; Pan, C.; Hu, W.; Zhai, J.; Li, Z.; Wang, Z. L. Dynamic Real-Time Imaging of Living Cell Traction Force by Piezo-Phototronic Light Nano-Antenna Array. *Sci. Adv.* **2021**, *7* (22), 7738−7764.
(71) Clay, N. E.; Shin, K.; Ozcelikkale, A.; Lee, M. K.; Rich, M. H.; Kim, D. H.; Han, B.; Kong, H. Modulation of Matrix Softness and Interstitial Flow for 3D Cell Culture Using a Cell-Microenvironment-on-a-Chip System. *ACS Biomater. Sci. Eng.* **2016**, *2* (11), 1968−1975.
(72) Liang, Y.; Clay, N. E.; Sullivan, K. M.; Leong, J.; Ozcelikkale, A.; Rich, M. H.; Lee, M. K.; Lai, M. H.; Jeon, H.; Han, B.; Tong, Y. W.; Kong, H. Enzyme-Induced Matrix Softening Regulates Hepatocarcinoma Cancer Cell Phenotypes. *Macromol. Biosci.* **2017**, *17* (9), No. 1700117.

https://doi.org/10.1021/acsnano.3c07527
ACS Nano 2023, 17, 25014−25026